On the Li-storage Capacity of SiOC Glasses with and without Mixed Silicon Oxycarbide Bonds

Magdalena Graczyk-Zajac[1], Dragoljub Vrankovic[1], Philipp Waleska[2], Christian Hess[2], Pradeep Vallachira Sasikumar[1§], Stefan Lauterbach[3], Hans-Joachim Kleebe[3] and Gian Domenico Sorarù[4]*

[1] Materialwissenschaft, Technische Universität Darmstadt, Otto Berndt Str. 2, 64287 Darmstadt, Germany

[2] Eduard-Zintl-Institut für Anorganische Chemie und Physikalische Chemie, Technische Universität Darmstadt, Alarich-Weiss-Str. 8, 64287 Darmstadt, Germany

[3] Institute for Applied Geosciences, Technische Universität Darmstadt, Schnittspahnstr. 9, 64287 Darmstadt, Germany

[4] Dipartimento di Ingegneria Industriale, Università di Trento, Via Sommarive 9, 38123 Trento, Italy

*corresponding author *soraru@ing.unitn.it*

[§]present address: Laboratory for High Performance Ceramics, EMPA, Dübendorf, Switzerland

Abstract

In this work we investigate the electrochemical behaviour of two silicon oxycarbide (SiOC) glasses synthesized from the same starting precursor. In one case we perform the pyrolysis in Ar flow, while in the second case, the glass is synthesized under CO_2 flow. The microstructural characterization of the glasses unambiguously demonstrates that the Ar-pyrolyzed material (SiOC-Ar) is a $SiOC/C_{free}$ nanocomposite with mixed SiC_xO_{4-x} $0 \leq x \leq 4$ units, whereas the CO_2-pyrolyzed sample (SiOC-CO_2) is a SiO_2/C_{free} nanocomposite with *exclusively* SiO_4 units forming the amorphous network. Therefore, in this study we investigate two model systems, addressing the question as to whether the mixed SiC_xO_{4-x} units in the SiOC glass play an essential role regarding electrochemical performance. The UV-Raman analysis reveals that the sp^2 carbon present in the mixed bonds-containing sample is more disordered/defective than the one dispersed into the SiO_2 matrix. Apart from the above dissimilarities, the materials present comparable microstructures and a similar amount of free carbon. Nevertheless, SiOC-Ar recovers almost twice higher reversible Li-ion storage capacity than SiOC-CO_2 (325 vs 165 $mAh \cdot g^{-1}$, respectively). We rationalize this difference in terms of the enhanced Li-ion storage in the more disordered free carbon phase of SiOC-Ar, while this disorder is induced by the presence of the mixed-bonds units.

1. Introduction

Li-ion batteries are widely used in portable electronics such as mobile phones, laptops and are now slowly entering the automotive market [1, 2]. Graphitic anodes provide stability and safety but the capacity does not exceed the theoretical value of 372 $mAh \cdot g^{-1}$. However, in order to meet the consumer requirements for lighter, higher capacity and faster charge/discharge systems, there is a strong interest in developing new materials, which can achieve such targets [3-5]. Among many different Li-ion storage hosts silicon, oxycarbide glasses, SiOCs, have attracted much attention recovering capacity up to 900 $mAh \cdot g^{-1}$ in line with the excellent stability against high rate tests and prolonged cycling[6-12].

Silicon oxycarbides belong to the family of Polymer Derived Ceramics (PDC), which are obtained from preceramic polymers through a pyrolysis process in controlled atmosphere [13]. SiOC glasses are derived from crosslinked polysiloxanes. The polymer structure is based on a Si-O-Si tridimensional network with organic moieties, such as $-CH_3$ or $-C_6H_5$ directly bonded to the silicon atoms [14, 15]. Upon pyrolysis at T ≥ 800 °C in inert atmosphere these precursors form a silicon oxycarbide network made of Si-centered tetrahedral sites with O and C atoms sitting at the corners bridging 2 or more Si-tedrahedra [16]. Part of the C atoms, initially belonging to the organic moieties, is converted into a separate sp^2 C phase, usually called "free carbon" phase. The chemical composition of the SiOC glasses can be expressed as: $SiC_xO_{2(1-x)} + yC_{free}$ where $SiC_xO_{2(1-x)}$ represents the chemical composition of the amorphous network and yC_{free} the molar amount of the free carbon phase [17].

When tested as Li-ion storage hosts, SiOCs glasses have shown very high *reversible* capacities up to 900 $mAh \cdot g^{-1}$ with a high rate capability, which allows to recover up to 200 $mAh \cdot g^{-1}$ at 2C rate (charge/discharge in 30 minutes) [18]. The performance of a composite materials consisting of SiOC and graphene is even better with reversible capacities of ~200 $mAhg^{-1}$ stable over 1000 cycles at 5C rate (charge/discharge in 12 minutes) [12, 19]. The drawback of SiOC anodes resides is the high first cycle irreversibility, which is around 30% in the best case, and the large hysteresis since the stored lithium ions are recovered at higher potentials thereby leading to the limited electrochemical performance of the cell [20-22]. The mechanism of Li-storage in SiOCs has not been fully rationalized yet. Obviously, a better understanding of the Li storage sites in silicon oxycarbides will be of a vital importance for overcoming the existing limitations of this electrode type while maintaining its advantages compared to the commercial graphite anodes. In the literature different hypothesis to explain how lithium atoms are stored in SiOCs have been presented including: (i) intercalation between the sp^2 C layers [8, 23, 24], (ii) the edges and micropores of neighboring graphene layers [23, 25] and (iii) in the Si-O-C glass phase [26], and in particular the mixed silicon oxycarbide units [27]. According to the results of ab-initio studies, mixed Si units impact Li insertion in SiOC by lowering the chemical potential (energy levels) of unfilled carbon electronic states [28-30].

Discerning between these hypotheses is not an easy task provided that the structure of silicon oxycarbide glasses is rather complicated, not yet fully understood, and it depends on many experimental parameters such as the composition of the precursor, the pyrolysis conditions (heating rate, maximum pyrolysis temperature, atmosphere), etc..

Recently, the group of Narisawa at Osaka Prefecture University showed that a commercial polysiloxane resin, which upon pyrolysis in argon flow would lead to the known silicon oxycarbide structure, namely $SiC_xO_{2(1-x)} + yC_{free}$, upon pyrolysis in CO_2 flow however leads to a SiO_2/C_{free} nanocomposite in which no Si-C bonds are present [31]. In other words, pyrolysis in CO_2 flow results in the complete cleavage of the Si-C bonds and at the end only SiO_2 and free carbon are present in the ceramic residue.

These findings give us an excellent opportunity to investigate the role of Si mixed bonds in the electrochemical storage of Li ions. Accordingly, we have synthesized two silicon oxycarbides from the same starting precursor: in one case we performed the pyrolysis in inert atmosphere, namely Ar flow and in the second case the precursor was pyrolyzed in CO_2 flow with the aim to prepare two

SiOC glasses having similar amount and distribution of free carbon in a (i) silicon oxycarbide matrix and (ii) silica matrix. Further, we rationalize the electrochemical performance of SiOC-Ar and SiOC-CO_2 with respect to their microstructural properties, and in particular the presence/absence of the mixed O-Si-C bonds.

2. Experimental Part

2.1 Synthesis of the SiOC glasses

In this work the starting precursor has been prepared in the form of a highly porous polysiloxane colloidal aerogel in order to facilitate the diffusion and reaction of the flowing CO_2 during the pyrolytic transformation. Indeed, it was shown by Narisawa et al. that, in order to have a complete reaction between the flowing gas and the preceramic polymer, the polysiloxane particle size must be below a few microns [32]. Poly(methylhydrosiloxane) (PMHS, CAS # 63148-57-2) and divinylbenzene (DVB, 80%, mixture of isomers, CAS # 1321-74-0) were purchased from Alfa Aesar (USA). Platinum(0)-1,3-divinyl-1,1,3,3-tetramethyldisiloxane complex solution ~Pt 2% in xylene (CAS # 68478-92-2) was obtained from Sigma-Aldrich (USA). All reagents were used as received. PMHS and DVB were mixed in a 1:2 weight ratio in acetone with an 80% (vol/vol) dilution. In a typical synthesis 0.8 g of PMHS, 1.6 g of DVB, and 8 g of acetone were mixed together in a Teflon container, stirred for about 10 minutes and then 19 µl of Pt catalyst were added. The crosslinking reaction was performed in a pressure vessel at 120 °C for 6 h. After 6 h of curing, the gels were allowed to cool down to room temperature, carefully removed from the Teflon container and transferred to solvent (acetone) to remove the unreacted polymer and catalysts by changing the acetone twice a day for five days. Wet gels were then supercritically dried in CO_2 using a home-made reactor at 50 °C and 100 bar.

The monolithic precursor gels were converted into the corresponding monolithic SiOC-Ar and SiOC-CO_2 glasses through a pyrolysis process at 900 °C for 1 h, using an alumina tubular furnace (Lindbergh blue) with a heating rate of 5°C/min and 100 ml/min of Ar or CO_2 flow, respectively.

2.2 Structural and microstructural characterization

The amount of carbon present in the pyrolyzed SiOC samples was measured by hot-gas extraction, using a Leco-200 carbon analyzer. The amount of free carbon in the SiOC glasses was also estimated by thermogravimetric analysis (TGA) in flowing air. Thermogravimetric analysis (TGA) was recorded on small aerogel fragments with a Netzsch STA 409 equipment (Netzsch Geraetebau Gmbh, Selb, Germany) at 5 °C/min in air flow (30 cc/min) up to 1300 °C.

The specific surface area (SSA), porosity and pore size of the precursor and of the two SiOC aerogels was investigated by N_2 physisorption using a Micromeritics 2010 ASAP instrument (Micromeritics, Norcross, GA, USA). N_2 isotherms were collected at 77 K after degasing at 200 °C for 4 h. The specific surface area was determined from a BET (Brunauer, Emmet, and Teller) analysis in the P/P_0 range of 0.05–0.30 using a molecular cross sectional area for N_2 of 0.163 nm^2 and a minimum of five data points. The pore size distribution (PSD) curves were evaluated using the BJH (Barret, Joyner, and Halenda) analysis from the desorption isotherm. The bulk density was determined on bulk cylindrical samples measuring the mass with an analytical balance and the dimensions with a caliper.

Micro-Vis-Raman spectra were recorded with a confocal micro-Raman spectrometer (Horiba HR 800, Horiba, Japan), using an Ar-Ion laser with a wavelength of 514.5 nm. Spectra were recorded in a Raman shift range from 0 to 4000 cm^{-1}.

UV Raman Spectroscopy has been carried out using a tunable Ti:Sa solid state laser (Coherent, Indigo-S) and a triple stage spectrograph (Princeton Instruments, TriVista 555) with an attached CCD camera (Princeton Instruments, Spec10:2kBUV). The tunable laser system has been adjusted to

a wavelength of 256.7 nm (THG). The spectral resolution of the spectrometer is 1 cm^{-1}. All UV Raman spectra were collected under ambient conditions at room temperature (≈25 °C) using a laser power of 3.6 mW. Laser damages can be excluded, because the radiation is only softly focused on the surface of the sample creating a spot size of about 0.6 mm^2 [33].The acquisition time of each spectrum was ≥ 1 h to obtain a sufficient signal-to-noise.

The first order regime is comprised of the G band (perfect carbon lattice) and the D/T/D'' band (**Table 1**), caused by deviation from the perfect graphitic lattice. Their respective appearance and intensity can provide important information about the molecular structure [34, 35].

Table 1. Selected Raman bands of carbonaceous materials

G band	≈ 1580 cm^{-1}	In-plane breathing mode of hexagonal sp^2-carbon rings (E_{2g} symmetry)
D band (D1)	≈ 1380 cm^{-1}	Disordered graphitic lattice, graphene layer edges/defects (A_{1g} symmetry), turbostratic carbons
D2 band	≈ 1620 cm^{-1}	Disordered graphitic lattice, (E_{2g} symmetry), in UV-Raman this bands corresponds to C-C configurations with a wider electronic gap [35, 36]
D3 band	≈ 1500 cm^{-1}	Amorphous carbon

In order to prepare the aerogels for the TEM measurement, a small quantity of both SiOC powder samples was dispersed in ethanol using an ultrasonic bath. The suspension was transferred into a caved tip with a pipette and then sprayed onto a thin amorphous carbon film, suspended on standard 300 mesh Cu TEM grids, using an ultrasonic vaporizer. The grid was dried under vacuum and cleaned in Ar-plasma for 20 s before it was transferred into the TEM column. No light carbon coating was applied, since one focus of the TEM investigations was to image the free-carbon phase. Phase contrast HRTEM was carried out employing a JEOL 2100 F (JEOL, Tokyo, Japan) transmission electron microscope equipped with a field emission gun, operated at 200 kV.

Chemical bonds present in the pyrolyzed SiOC samples were investigated by Fourier Transform Infrared (FT-IR) spectroscopy. FT-IR spectra were collected in transmission mode using a Varian 4100 FT-IR Excalibur Series equipment in the range 4000–400 cm^{-1} with KBr pellets. An average of 50 scans with a resolution of 2 cm^{-1} were recorded for each sample.

The local environment around the silicon atoms was investigated by ^{29}Si solid state nuclear magnetic resonance (^{29}Si SS-NMR). The analyses were carried out with a Bruker 300WB instrument operating at a proton frequency of 300.13 MHz. NMR spectra were acquired with a SP pulse sequence under the following conditions: ^{29}Si frequency: 59.60 MHz, π/4 pulse length: 2.25µs, recycle delay: 150 s, 4k scans. Samples were packed in 4 mm zirconia rotors, which were spun at 5 kHz under air flow. Q8M8 was used as external secondary reference.

2.3 Electrochemical characterization

To prepare electrodes, the pyrolyzed SiOC samples were mixed with carbon black (Super P) and polyvinylidene fluoride binder (85:5:10 by weight) in N-methyl-2-pyrrolidone to form a slurry. This slurry was then coated onto a copper foil using a doctor blade and dried at 40 °C for 24 h. Electrodes of 10 mm diameter were cut out of the coated copper foil, and dried at 80 °C under vacuum in a Buchi oven for 24 h. Without further contact to air the dried electrodes were transferred to an argon-filled glove box for cell assembly (Swagelok® type cell) using lithium foil as the counter electrode and QMA (Whatmann™, UK) as a separator. As electrolyte 180 µl of 1 M $LiPF_6$ dissolved in in the commercial electrolyte EC:DMC/1:1 (Solvionic, France) was used. All cells were cycled at charging/discharging rates of 36 $mA \cdot g^{-1}$ between 0.005 and 3V *versus* Li/Li^+.

3. Results and discussion

3.1 Electrochemical results

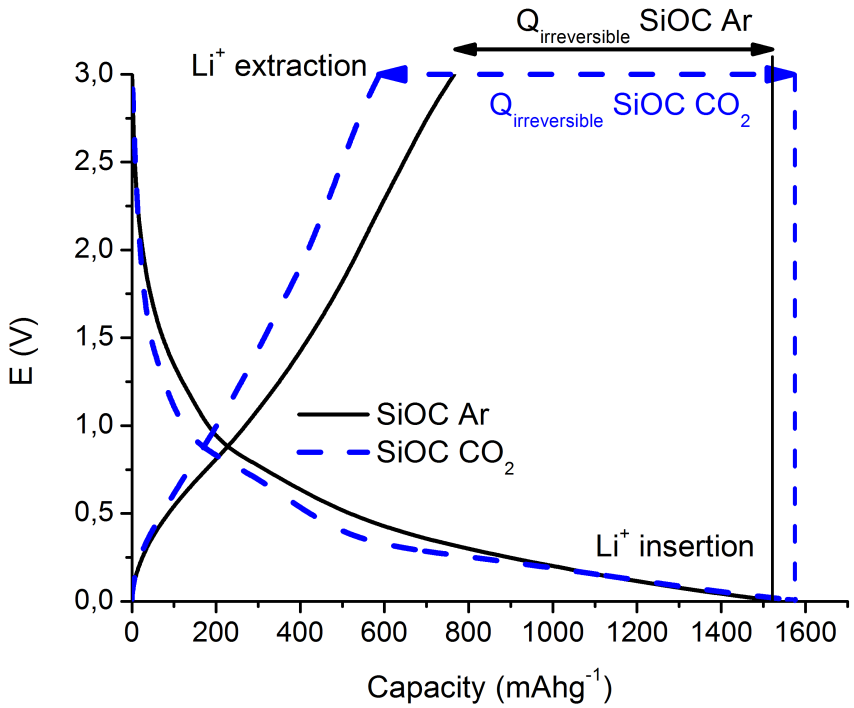

Figure 1 First cycle of the galvanostatic insertion / extraction of lithium ion into SiOC-Ar and SiOC-CO_2.

The first insertion/extraction of lithium ions into SiOC-Ar and SiOC-CO_2 is depicted in **Figure 1**. As a first observation we can say that the charging and discharging curves reveal only small differences. During the first lithiation, a continuous slope of the curve is found for SiOC-Ar. This slope is typical for silicon oxycarbide glasses, namely for SiOC glasses containing mixed SiC_xO_{4-x} $0 \leq x \leq 4$ sites, and it has been reported and discussed by us elsewhere [9, 11, 37]. In the lithiation of the CO_2-treated aerogel a plateau-like slope at 0.25 V can be found. Since this sample is a SiO_2/C_{free} nanocomposite (as will be shown later on), we tentatively attribute this plateau to hardly reversible storage of lithium ions in the silica network. Due to the porous morphology of both samples (the corresponding experimental results of N_2 adsorption will be addressed in the following paragraph) the losses related to a solid electrolyte interface (SEI) formation (0.6–2 V) are pronounced. Although the SSA of SiOC-CO_2 is almost twice higher than that of SiOC-Ar, there is no significant difference in the charge lost in this potential range. This feature can be rationalized recalling that the CO_2-treated sample is indeed a SiO_2/C composite and silica does not contribute to the formation of the SEI. Moreover, HRTEM investigations (for details, see Figure 8) revealed that for the Ar-treated samples the surface of the individual aerogel particles is covered by a continuous C film, while for the CO_2-treated aerogel the C film is no more continuous leading to the exposition of the SiO_2 to the electrolyte. Therefore, the absolute surface areas efficiently covered by carbon are almost similar in these samples.

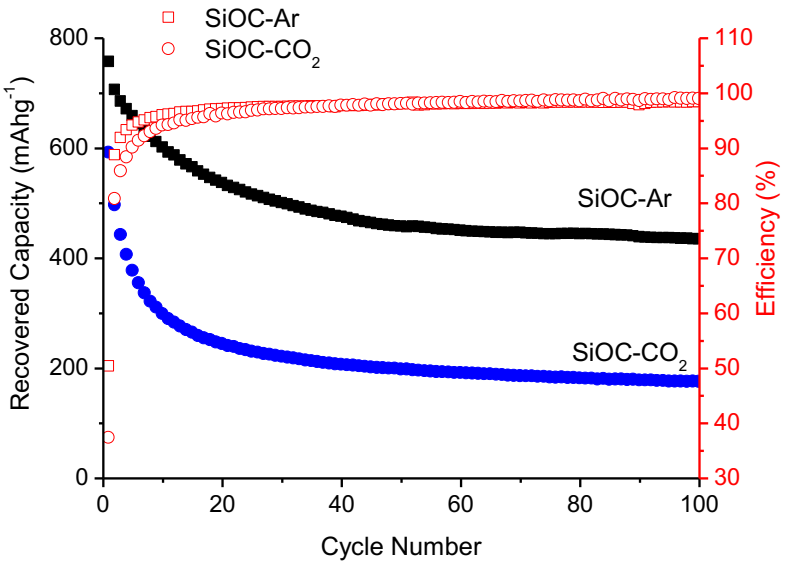

Figure 2: Capacity recovered during the extended galvanostatic cycling of SiOC-Ar and SiOC-CO_2

Figure 2 presents the prolonged galvanostatic cycling of the SiOC-Ar and SiOC-CO_2 samples. Although the first lithiation capacities are similar (compare Figure 1) and the charge recovered in the few initial cycles tends to fade, the stabilized capacity values of SiOC-Ar are almost twice as high as for SiOC-CO_2. ***This is the most important difference we found in the two studied samples and hereafter we will discuss and relate this finding with respect to the different chemical structures of the investigated glasses.***

3.2 N_2-adsorption measurements

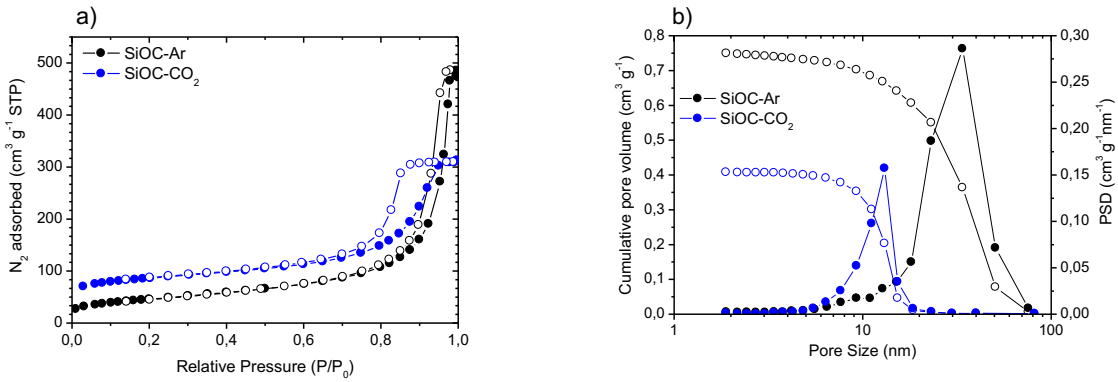

Figure 3: (a) Adsorption (solid circles)/desorption (empty circles) isotherms recorded on the SiOCs aerogels; (b) cumulative pore volume (open circles) and pore size distribution (PSD, solid circles)

We performed a careful structural and microstructural characterization of the two investigated materials to reveal the reasons of the pronounced difference in the electrochemical performance of SiOC-Ar and SiOC-CO_2 glasses. **Figure 3** presents the results of the N_2 physisorption analysis, while the relevant values are reported in **Table 2**.

Table 2. Porosity data on SiOC-Ar and SiOC-CO_2 aerogels.

Sample	T (°C)	Density ($g \cdot cm^{-3}$)	SSA ($m^2 \cdot g^{-1}$)	Pore volume ($cm^3 \cdot g^{-1}$)	Pore size (nm)
SiOC-Ar	900	0.47	163	0.75	20-50
SiOC-CO_2	900	0.48	279	0.41	7-20

SiOC-Ar and SiOC-CO_2 glasses show Type IV adsorption/desorption isotherms typical for mesoporous materials (Figure 3a) with a hysteresis loop in the 0.8-0.9 P/P_0 range. SiOC-Ar reveals a total pore volume of 0.75 $cm^3 \cdot g^{-1}$ and a maximum of the pore size distribution curve in the range 30-40 nm, (Figure 3b). The pyrolysis in CO_2 flow leads to a mesoporous aerogel with lower amount of total porosity (0.41 $cm^3 \cdot g^{-1}$) and smaller pore size with a maximum around 10-12 nm. Due to the contribution of the smaller pores, the specific surface area of SiOC-CO_2 is higher compared to the sample treated in Ar flow.

3.3 ^{29}Si solid-state NMR and FT-IR spectroscopy

The ^{29}Si SS-NMR and FT-IR spectra recorded on the SiOC-Ar and SiOC-CO_2 aerogels are shown in **Figure 4**.

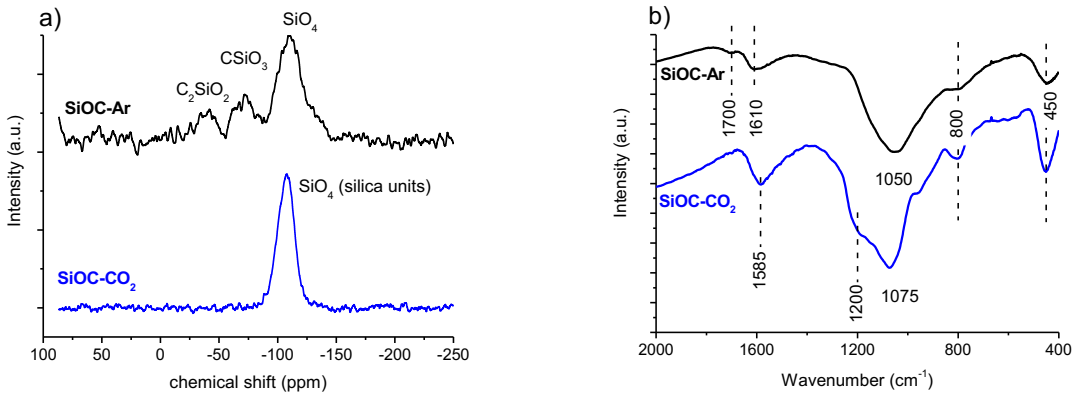

Figure 4: (a) ^{29}Si SS NMR and (b) FT-IR spectra recorded on SiOC-Ar and SiOC-CO_2.

The ^{29}Si SS NMR spectrum of the Ar-treated sample shows the presence of resonances at -39, -71 and -110 ppm assigned to mixed C_2***Si***O_2, C***Si***O_3 and ***Si***O_4 Si sites, respectively, which are typical of a silicon oxycarbide glass [38]. On the contrary, the spectrum of the sample pyrolyzed in CO_2 flow shows only resonance at -107 ppm, typical for SiO_4 units of silica glass. Thus, the NMR study unambiguously proves that, as expected, the pyrolysis in CO_2 flow changed radically the structure of the SiOC glass by consuming all Si-C bonds and converting them into Si-O bonds. FT-IR spectra support the findings obtained by ^{29}Si SS-NMR. The FT-IR spectra of both, SiOC-Ar and SiOC-CO_2, show peaks related to the presence of Si-O bonds in the range 1100-1000 cm^{-1} and at 450 and 800 cm^{-1}. The main peak corresponding to the stretching of the Si-O-Si bonds is located at 1050 cm^{-1} for the SiOC-Ar sample and at 1075 cm^{-1} for the SiOC-CO_2 aerogel. According to the literature, the shift toward lower wavenumbers (observed for SiOC-Ar) is associated with the insertion of C atoms into the silica network and a corresponding increase of the Si-O-Si bond angle above 150° [39]. On the other hand, the position at 1075 cm^{-1} for the stretching of the Si-O-Si bonds in SiOC-CO_2 confirms the formation of a SiO_2 network [31, 40]. In conclusion, both NMR and FT-IR spectroscopies clearly confirm that, upon pyrolysis in CO_2 flow, the silicon oxycarbide network is transformed into a silica network. The FT-IR spectra of both materials also show a peak around 1600 cm^{-1}. It is assigned to the vibration of C=C bonds of the C_{free} phase [40, 41]. The peak at 1600 cm^{-1} is more intense in case of the CO_2-treated sample suggesting either a higher amount of C_{free} or a better organized structure compared to the Ar-pyrolyzed aerogel. Finally, in the SiOC-Ar sample, the IR also reveals an absorption at 1700 cm^{-1} which indicates the presence of C=O bonds [40, 41]. C=O moieties could be formed, either during the pyrolysis process or after pyrolysis by exposing the aerogel to ambient conditions [42]. Assuming that the C=O bonds, observed in the Ar-treated sample, are formed after exposing the pyrolyzed aerogel to the laboratory atmosphere, then this would suggest that the Ar-pyrolyzed aerogels are more reactive compared to those pyrolyzed in CO_2.

Chemical analysis revealed that the total amount of C present in the SiOC aerogels amounts to 45 and 33 wt.% for the SiOC-Ar and the SiOC-CO_2 sample, respectively. Since for the CO_2-treated sample C is present only in the C_{free} phase, this amount (33 wt.%) represents the amount of segregated carbon. For the SiOC-Ar sample the evaluation of the free carbon amount is not straightforward since a part of the C atoms is engaged to form Si-C bonds. We can only infer that the amount of segregated C in SiOC-Ar must be lower than 45 wt.%. We also performed thermogravimetric analysis in air to assess the amounts of the free carbon phase. The corresponding TGA curves are depicted in Figure 5.

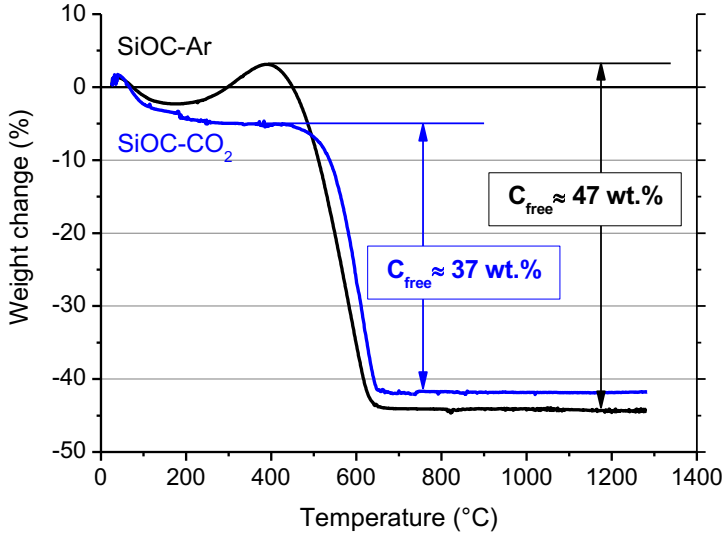

Figure 5: TGA in flowing air on the SiOC-Ar and SiOC-CO_2 aerogels.

Both curves show an initial small weight loss below 200 °C due to the evaporation of adsorbed water. For the SiOC-CO_2 sample the weight is stable up to 450 °C. At ~500 °C the C_{free} is oxidized according to the reaction $C + O_2 \rightarrow CO_2$, leading to a weight loss of 37 wt.%.

Compared to the value of C measured by chemical analysis the result from TGA analysis seems to be overestimated. This discrepancy could be, at least partially, explained by considering that the sp^2 C phase in the silicon oxycarbide glass, pyrolyzed at relatively low temperature (900 °C), may still contain hydrogen, which also contributes to the measured weight loss. In conclusion, the amount of C_{free} estimated by TGA for the CO_2-treated sample (37 wt.%) can be considered as an upper limit.

The TGA curve of the Ar-treated sample shows first a small increase (~6 wt.%) in the temperature range between 250 and 400 °C. This feature is related to the oxidation of Si-CH_x (x = 1, 2) bonds leading to new Si-O/Si-OH bonds resulting in a corresponding net weight increase [40]. For this sample oxidation of C_{free} leads to a weight loss of 47% at temperatures between 400 and 650 °C. Also for SiOC-Ar, the amount of the sp^2 C phase may be overestimated due to the likely presence of residual hydrogen in the pyrolyzed aerogel.

In summary, the TGA results confirm the absence of Si-C bonds in the CO_2-pyrolyzed material and suggest that the SiOC-Ar sample contains slightly more free carbon than the CO_2-treated aerogel.

3.4 UV/Vis-Raman spectroscopy

The Vis-Raman spectra are presented in Figure 6. The D mode present at around 1335 cm^{-1} originates from disorder-induced breathing motions of six-fold aromatic rings, whereas the G mode at around 1590 cm^{-1} is induced by in-plane bond stretching of sp^2 hybridized C atoms. The 2D bands at around 2700 cm^{-1} and 3200 cm^{-1} are attributed to second-order vibration modes of the D band.

The Raman band at around 2940 cm^{-1} is the D+G combination mode induced by carbon disorder [35]. The strong fluorescence at higher wavenumbers (beyond 2000 cm^{-1}) registered for the SiOC-Ar sample is associated with the higher amount of defects present in the sample or/and organic residues, e.g. radicals such as $C^{\bullet}$, $CH^{\bullet}$ [43]. Nevertheless, the results of the carbon bands fitting performed according to Sadezky et al. showed no significant difference in the carbon microstructure of the investigated aerogels [34].

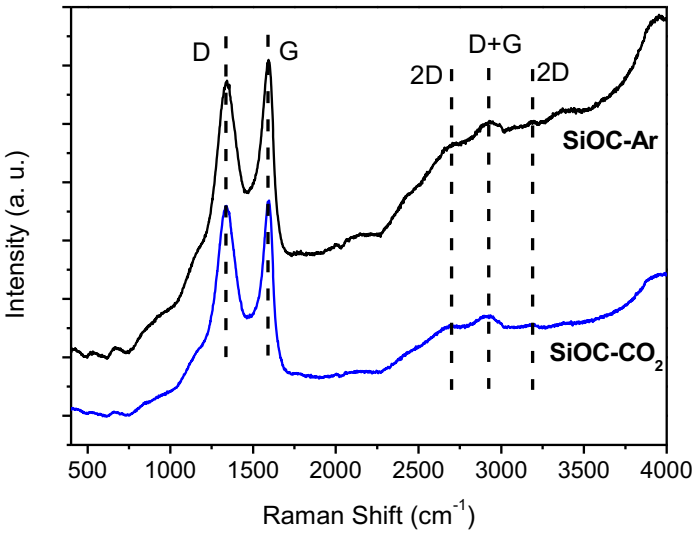

Figure 6 Vis-Raman spectra of the samples pyrolyzed under Ar and CO_2

In order to access subtle differences in the free carbon phase within the investigated aerogels, UV-Raman spectroscopy was performed. UV Raman, by exciting both π and σ-states, allows to probe highly disordered/clustered carbons. The first order UV Raman spectra of SiOC-Ar and SiOC-CO_2 together with the results of a peak-fit analysis are plotted in Figure 7 a and b, respectively. For closer examination of the wavelength interval between 1000 cm^{-1} and 2000 cm^{-1} a fitting procedure considering the G-band and three D-bands (D, D2, D3) was applied. The assignment of the bands to the related vibrations/carbon form is addressed in the experimental section (see Table 1). The used line profiles were adopted from extensive studies on carbons by Sadezky et al. and Ferrari et al. [34, 35] (see Table 3). The D-band, which is related to the disordered graphitic lattice caused by defects on the edges of the turbostratic carbons, is very broad (although of low intensity). The G-band is comparably less pronounced confirming a low degree of graphitic order in the carbon phase. The D3-band indicates the presence of amorphous carbon. Its low intensity points out the turbostratic character of the free carbon phase. Both aerogels reveal a D2-band with the highest intensity, confirming the presence of a disordered graphitic lattice. Since this band is absent in the Vis-Raman spectra of the aerogels, we first try to assign it to the corresponding carbon form/hybridization. Sadezky et al. reported that in polycrystalline graphite the D2 band is usually of weak intensity, however, it becomes strong in soot-like materials. Castiglioni et al. [36, 44] investigated polyconjugated molecules, polycyclic aromatic hydrocarbons (PAHs), characterized by a planar network of sp^2 carbon atoms with the same relative arrangement shown by carbon atoms in a graphite sheet. These molecules are considered as molecular models of the graphitic 'islands' of finite size, which are expected to occur in disordered and nanostructured carbon materials containing sp^2 carbons. The presence of bands over 1600 cm^{-2} has been observed experimentally and modelled for these polyaromatic structures [36]. We do not expect such organic structures in the aerogels pyrolyzed at 900 °C, but we rationalize the appearance of a strong D2 band for higher excitation energy (UV laser) by considering the presence of small, microcrystalline graphitic domains. Graphitic domains of a given size are characterized (in a similar way as in the case of molecules) by a non-vanishing energy gap related to the electronic excitation localized on the domain. The frequency of the

Raman bands is also size dependent (as shown by the study on molecules [44]) and therefore dependent on the energy gap. Raman experiments carried out at different excitation energies [35, 45, 46] on a disordered sample containing a distribution of different graphitic domains extract the response of those domains, which satisfies the resonance condition ($E_{gap} \approx hv_{laser}$). In other words, while changing the laser energy one probes different "confined" structures. Using the above reasoning, we conclude that the D2-band originates from small clusters of sp^2 hybridized carbons characterized by a wide energy gap. Thus, those clusters can only by analysed using UV-excitation.

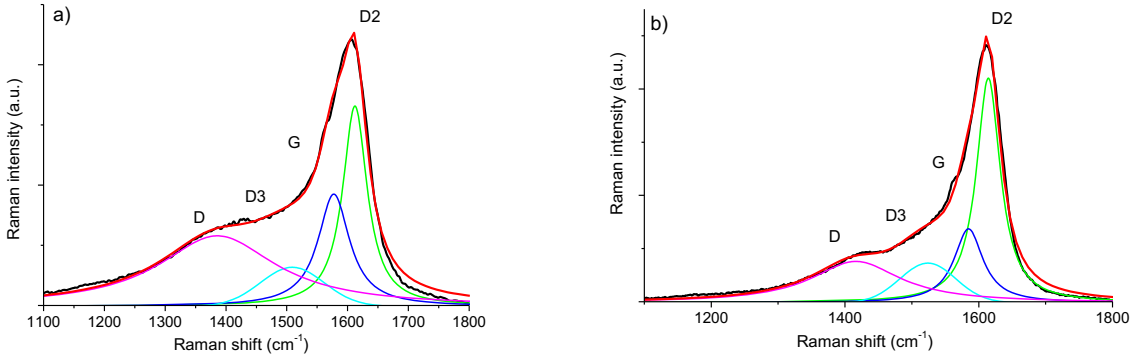

Figure 7 First order UV-Raman spectra of (a) SiOC-Ar and (b) SiOC-CO_2 together we the results of peak-fit analysis.

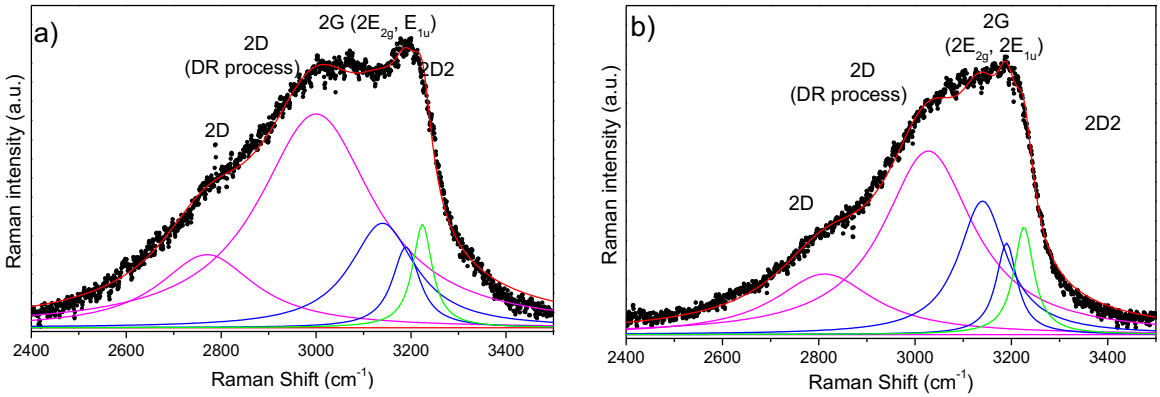

Figure 8 Second order UV Raman spectra of (a) SiOC-Ar and (b) SiOC-CO_2 together we the results of peak-fit analysis. A background subtraction was performed for all spectra.

Figure 8 presents the second order Raman spectra of SiOC-Ar and SiOC-CO_2. At first glance, the second order spectrum of SiOC-Ar reveals a significant broadening around 2800 cm^{-1} in comparison to the spectra of the CO_2 pyrolysed aerogel. For further analysis both spectra are fitted with Lorentzian shaped profiles according to Tyborski et al. **[47].** Deconvolution of the Raman spectra yields five contributions located at ~2800, ~3000, 3140, 3190 and 3225 cm^{-1}. With the exception of the signal at ~3000 cm^{-1} all bands are assigned to overtones related to signals in the fundamental region of the Raman spectrum. In detail, the features at 3140 and 3190 cm^{-1} are assigned to overtones of the G-band (E_{2g} and E_{1u}). The latter overtone belongs to an infrared-active fundamental. It becomes detectable in the Raman spectrum, because the decomposition of the direct product E_{1u} x E_{1u} contains always the fully symmetric representation **[47]**. The two signals at 2800 and 3230 cm^{-1} are assigned to overtones of the D and the D2-bands, respectively. The broad and intense feature at around 3000 cm^{-1} is also related to the D band, as discussed by Tyborski *et al*. Accordingly, this feature is uniquely formed under UV excitation (4.83 eV) and originates from a double resonance effect involving an electronic transition as well as a resonance between two TO phonons at the M point of the phonon dispersion of graphite **[47].**

Table 3. Band assignment, positions and area contributions of the first order UV-Raman signals.

Raman band assignment First-order	SiOC-Ar		SiOC-CO_2	
	Position [cm^{-1}]	Peak area contribution [%]	Position [cm^{-1}]	Peak area contribution [%]
D	1385	44	1416	28
D3	1509	9	1523	12
G	1577	20	1584	17
D2	1612	27	1614	43

Table 4. Band assignment, positions and area contributions of the second-order UV-Raman signals.

Raman band assignment Second-order	SiOC-Ar			SiOC-CO_2		
	Position [cm^{-1}]	Peak area contribution [%]		Position [cm^{-1}]	Peak area contribution [%]	
2D	2770	16	74	2812	18	68
2D (DR process)	3000	58		3027	50	
E2g (2G band)	3140	16	21	3140	20	26
E1u (2G band)	3189	5		3190	6	
2D2	3224	5		3226	7	

The contributions of the first/second order Raman signals are listed in Table 3/Table 4, respectively. These contributions represent a quantitative estimation of the amount of carbon with the corresponding microstructure. In the first order spectra, a significant difference is found in the areal contribution of D and D2 band in dependence on the pyrolysis atmosphere. The contribution of D band in the SiOC-aerogel is 44%, whereas for SiOC-CO_2 the main contribution arises from the D2-band with 43%. The contributions of G and D3 bands are similar for both samples. In the second order spectra, the contribution of the defect overtones (2D bands) is higher for the SiOC-Ar in comparison to SiOC-CO_2 (74 vs. 68%, respectively) sample confirming the results of the analysis in the fundamental region [48]. The contributions of the 2D2-band amount to 5 and 7 % for SiOC-Ar and SiOC-CO_2, respectively. This difference is much less pronounced than in the fundamental region. Nevertheless, one has to keep in mind that in general the intensity of the second order bands is low. Thus, the fitting and quantitative interpretation of those signals are less conclusive.

Taking into account the above analysis/discussion of the peak area contributions and the origin of the band the following conclusion on the microstructure of the carbon phase within the studied aerogels can be drawn:

i) D band: SiOC-Ar is mostly (main contribution of D band, both in the first and in the second order spectra) composed of disordered/defected carbon (with traces of sp^3) with defects mainly concentrated at the edges of the sp^2 C planes. This implies that the carbon phase within the mixed-bonds SiOC is less ordered and more defected. The strong fluorescence, found in SiOC-Ar Vis-Raman spectra, associated with the presence of defects/radicals and C=O bonds as identified by means of FT-IR, supports the above statement. This conclusion is supported by both the fundamental and the overtone region.

ii) D2-band: The carbon phase of SiOC-CO_2 aerogel consists mostly (43%) of very small clusters of sp^2 hybridized carbon (possibly microcrystalline graphite). SiOC-Ar contains less small sp^2 clusters (27 %). This implies that, for CO_2-pyrolyzed aerogel, the carbon phase is better organized. This hypothesis is consistent with the analysis of the overtone region.

The formation of a more disordered C_{free} for the Ar-pyrolyzed aerogel and conversely of a more ordered free carbon phase for the CO_2-treated material supports the findings by the NMR study, which indicate the formation of a SiO_2 network without any Si-C bonds for the SiOC-CO_2 sample. Therefore, since in the SiOC-CO_2 sample the free carbon is not connected to the matrix via primary Si-C chemical bonds, it can more easily rearrange toward a more ordered carbon phase. On the other hand, in the Ar-treated material, Si-C bonds are present in the amorphous SiOC matrix. At this stage we do not have any experimental evidence that proves the existence of Si-C bonds at the SiOC/C_{free} interface but, at the same time, we cannot exclude it. Accordingly, if Si-C bonds exist at the interphase between the free carbon and the silicon oxycarbide matrix, then the rearrangement of the sp^2 C planes into a more ordered free carbon cluster will be more difficult.

3.5 TEM investigation

Representative TEM micrographs of the Ar- versus CO_2-treated SiCO sample are depicted in Figure 9. At first glimpse, both samples reveal a nearly identical microstructure: nanosized SiCO-particles attached to each other with also a nanosized porosity. However, the sample pyrolyzed in Ar shows a slightly larger individual porosity, as compared to the sample treated in CO_2 (Figure 9 a,b).

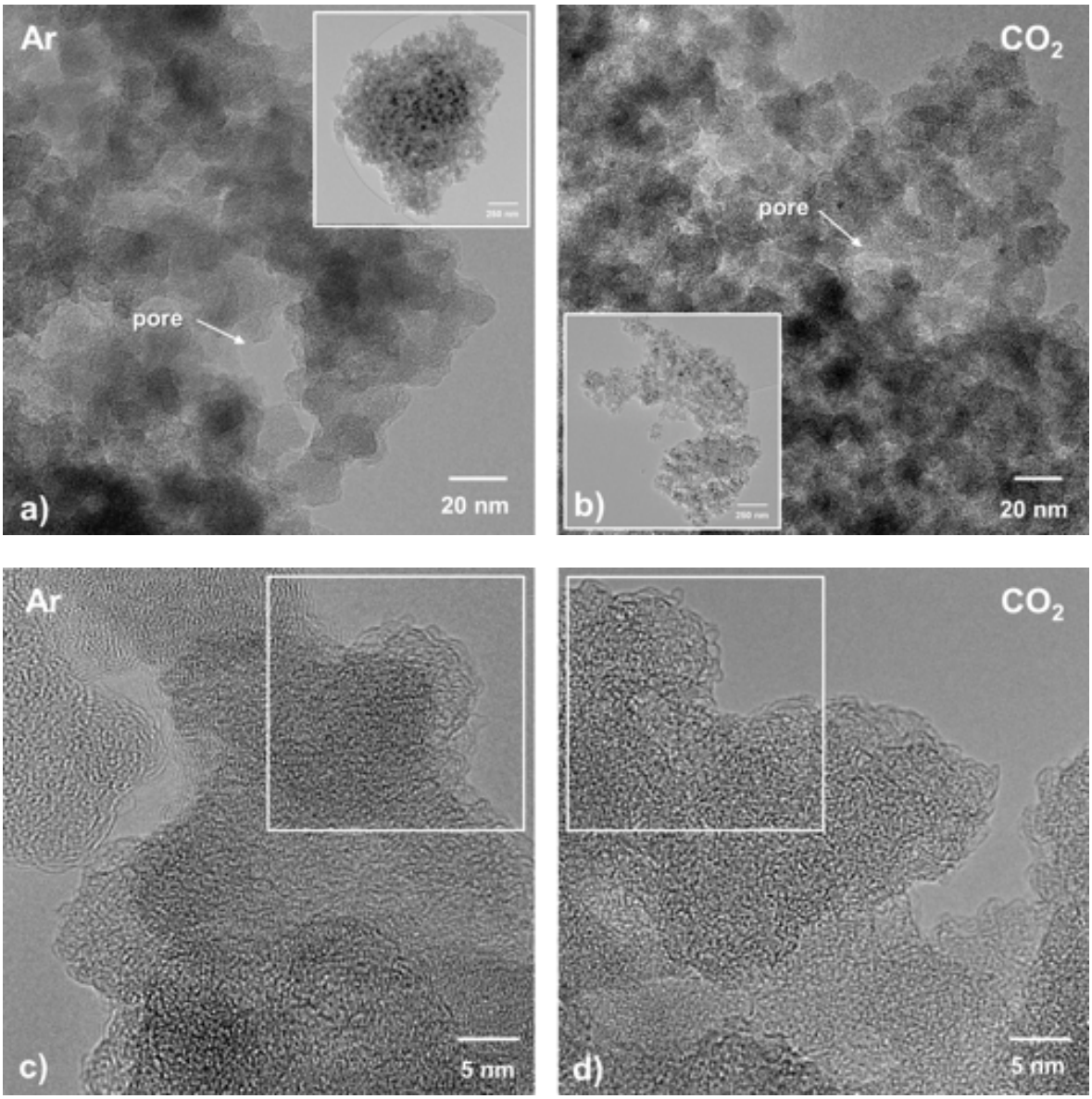

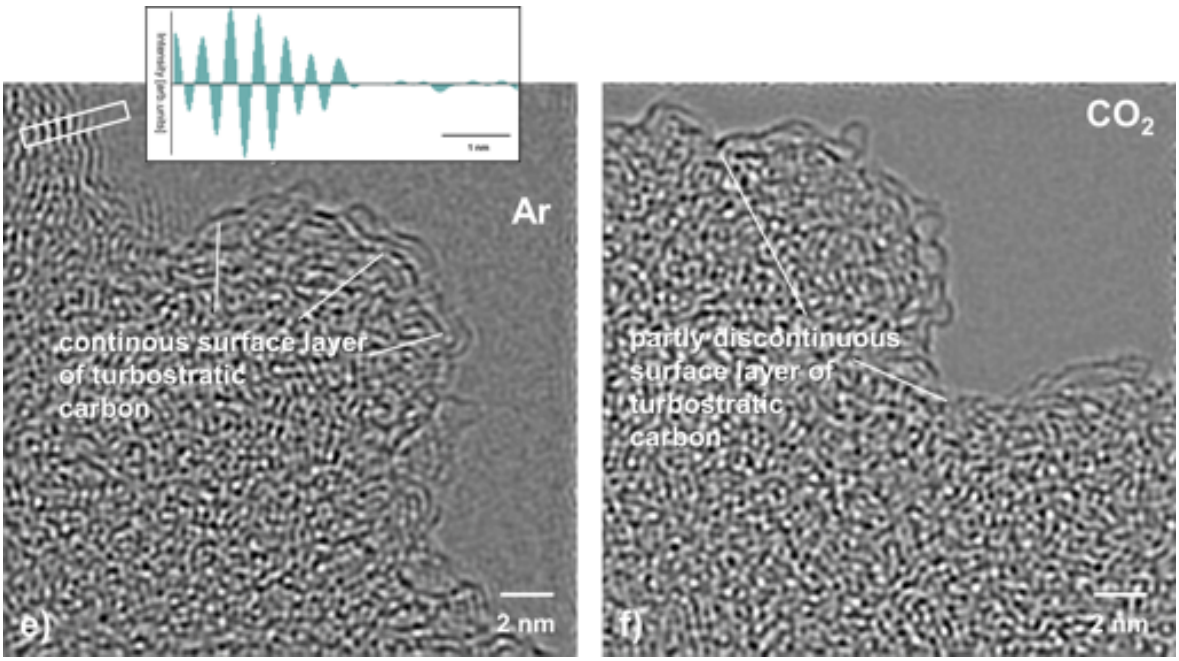

Figure 9 TEM micrographs revealing an overview of (a) SiOC-Ar and (b) SiOC-CO_2. The insets show characteristic powder particles. c) and d) are corresponding images at higher magnification, with a phase contrast typical for predominantly amorphous materials. e) and f) show Fourier-filtered HRTEM images from the boxed regions in c) and d), indicating the free-carbon phase at the outer surface of the SiOC matrix. Note that in case of Ar-treatment, there is a continuous turbostratic carbon film visible, while in the CO_2-treated material a partly discontinuous carbon film was observed. The inset in e) shows the intensity profile (boxed area) of the outer free-carbon film, which is rather thick in this region (SiCO-Ar).

At higher magnification, the observed phase contrast for both samples is characteristic for predominantly amorphous materials (Figure 8 c,d). From the corresponding Fourier-filtered HRTEM images (Figure 8 e,f) it becomes obvious that there is no visible free-carbon phase present within the SiOC host matrix, independent from the glass nature, i.e., SiOC with containing mixed SiC_xO_{4-x} sites versus a pure SiO_2 glass matrix. This is consistent with earlier studies on SiOC, where the formation of so-called basic structural units (BSU) was reported to be visible via TEM imaging upon pyrolysis above 1000 °C [49, 50]. However, in both samples there is a thin film of turbostratic carbon present, being continuous in the case of Ar-treatment, while it is partly discontinuous in the SiOC-CO_2 sample. It is assumed that the observed discontinuity originates from a surface reaction during pyrolysis of CO_2 with the carbon layer: $C + CO_2 \rightarrow 2CO$. Note that the free-carbon film is rather thick, compared to the CO_2-treated sample, as shown in the inset in Figure 8 e, revealing a spacing of the turbostratic carbon layers of approximately 0.23-0.24 nm, typical for disordered carbon.
The obtained TEM results clearly show that pyrolysis in different atmospheres does not significantly change the overall microstructure of SiOC, which is homogenous and predominantly amorphous in both cases. However, HRTEM confirms that the individual pore size is lower for the SiOC-CO_2 material as compared to the SiOC-Ar sample. The local distribution and size of the C_{free} phase is similar in both materials; i.e., a thin film of turbostratic carbon is present on the surface of the matrix particles. There is no evidence that pyrolysis in CO_2 atmosphere results in a local agglomeration of the free-carbon phase or phase separation of carbon within the matrix. The finding that the surface free carbon is partly discontinuous in the CO_2-treated sample is consistent with the lower amount of free carbon measured with different techniques as well as the slightly higher surface film thickness observed in the SiCO-Ar sample (Figure 9e).

3.6 Discussion

The ^{29}Si MAS NMR results unambiguously demonstrated that the Ar-pyrolyzed material is a SiOC/C_{free} nano-composite with mixed SiC_xO_{4-x} $0 \leq x \leq 4$ units present in the silicon oxycarbide network. On the other hand, the CO_2-pyrolyzed aerogel is a SiO_2/C_{free} nanocomposite with only SiO_4 units forming the amorphous network. The amount of free carbon, estimated by TGA, is comparable in the two materials with a slightly higher amount in the Ar-treated SiOC (~47 wt.%) compared to the CO_2-treated aerogel (~37 wt.%). CO_2 flow leads to a lower total pore volume with smaller pore size. In terms of specific surface area, however, the smaller pores result into a higher value of the SSA (259 m^2g^{-1} for SiOC-CO_2 vs 163 m^2g^{-1} for SiOC-Ar). The HRTEM study revealed for both samples a rather featureless microstructure, typical for predominantly amorphous materials. The free carbon phase, which is supposed to be finely dispersed into the amorphous matrix, is not detectable in both samples annealed at 900 °C. Therefore, the possibility that the pyrolysis in CO_2 flow will lead to a macroscopic phase separation of the free carbon phase within the SiO_2 glass matrix can be excluded. Additionally, the TEM investigation revealed the presence of a continuous C film at the surface of SiOC-Ar particles, while the carbon film present on SiOC-CO_2 is discontinuous. The UV-Raman analysis revealed that the sp^2 C present in the mixed-bonds containing samples is more disordered/defective than the one dispersed into the SiO_2 glass. We could infer that the mixed SiC_xO_{4-x} $0 \leq x \leq 4$ units, which are probably present not only in the amorphous SiOC network but also at the interface between the SiOC and the C_{free} layers, hinder the organization of the free carbon phase.

Until now, three electrochemically active sites for Li-ion storage have been experimentally identified within carbon-rich SiOC by ^{7}Li-MAS-NMR measurements [23, 51-53]. Accordingly, the major Li-ion host sites are interstitial spaces and edges of graphene and carbon layers within the free carbon phase. A minor storage contribution is assigned to less ionic Li-species that are stored in micropores and to diamagnetic Li-species that are directly or indirectly stored in the mixed SiOC network. Thus, let us first consider the sp^2 carbon as the only phase, which can reversible store Li-ions. The higher capacity observed for the SiOC-Ar samples might be attributed to the higher amount of C_{free}. However, the SiOC-Ar aerogel contain only ~10 wt% more free carbon than the SiOC-CO_2 sample (~47 wt.% for the SiOC-Ar vs 37 wt.% for the SiOC-CO_2) but display an almost doubled Li-storage reversible capacity. In our former work[9] we clearly showed that for the SiOC glasses containing more than 20 wt.% of the free carbon phase, the increasing amount of carbon hardly affects the Li-storage capacity. Therefore, the higher C_{free} content (wt.%) itself cannot rationalize the higher Li-storage capacity of the SiOC-Ar. As a consequence, we must assume that either (i) the capacity of the free carbon phase of the two composites is different (and in particular the capacity of the sp^2 C of the SiOC-Ar is higher than the one of SiOC-CO_2) or, (ii) the glass matrix itself provides additional sites to reversibly store lithium ions. The Raman spectroscopy study suggests that, indeed, the free carbon phase in the SiOC-Ar samples has a higher degree of disorder/defects compared to the "micrographitic" like C_{free} of the CO_2-treated samples. The more disordered carbon allows a higher capacity to store lithium, not only between the sp^2 C layers but also at the edge of the layers [37, 54]. In this case, the role of the mixed SiC_xO_{4-x} units present in the glassy matrix would lead to an indirect increase in the capacity by inducing the formation of a more disordered C phase.

Conclusions

Within this work we discussed the role of mixed SiC_xO_{4-x} $0 \leq x \leq 4$ sites with respect to their potentially high reversible Li-ion storage capacity. Two model systems were studied, a SiOC matrix with mixed units (SiOC-Ar) and a material with no such mixed structural units (SiOC-CO_2), where in the latter sample the matrix converted to pure SiO_2 upon pyrolysis. The mixed bonds present in the SiOC-Ar material induce (i) the formation of a more disordered/defective carbon phase, which thereby has a higher capacity for reversible storage of Li ions and/or (ii) directly provides reversible storing sites at the interface between the amorphous network and the free carbon. Hence, it can be concluded that there is indeed a pronounced effect of mixed units within the SiOC glass matrix on the Li-storage capacity of the material.

Acknowledgements

Dr. Emanuela Callone is gratefully acknowledged for performing the ^{29}Si SS NMR analyses using the equipment of the "Klaus Müller" NMR Lab. of the Industrial Engineering Department at the University of Trento. Mrs. Ababo Gudisa is gratefully acknowledged for the synthesis of the precursor and ceramic aerogels.

References

1. J. B. Goodenough and Y. Kim, *Chem. Mater.*, 2010, **22**, 587-603.
2. J. M. Tarascon, *Philos. Trans. R. Soc., A*, 2010, **368**, 3227-3241.
3. A. Magasinski, P. Dixon, B. Hertzberg, A. Kvit, J. Ayala and G. Yushin, *Nat Mater*, 2010, **9**, 353-358.
4. S. Goriparti, E. Miele, F. D. Angelis, E. D. Fabrizio, R. P. Zaccaria and C. Capiglia, *J. Power Sources*, 2014, **257**, 421-443.
5. P. Roy and S. K. Srivastava, *J. Mater. Chem. A*, 2015, **3**, 2454-2484.
6. W. Xing, A. M. Wilson, K. Eguchi, G. Zank and J. R. Dahn, *J. Electrochem. Soc.*, 1997, **144**, 2410-2416.
7. D. Ahn and R. Raj, *J. Power Sources*, 2011, **196**, 2179-2186.
8. M. Graczyk-Zajac, L. M. Reinold, J. Kaspar, P. V. W. Sasikumar, G.-D. Soraru and R. Riedel, *Nanomaterials*, 2015, **5**, 233-245.
9. J. Kaspar, M. Graczyk-Zajac, S. Choudhury and R. Riedel, *Electrochim. Acta*, 2016, **216**, 196-202.
10. M. Graczyk-Zajac, L. Toma, C. Fasel and R. Riedel, *Solid State Ionics*, 2012, **225**, 522-526.
11. J. Kaspar, M. Graczyk-Zajac and R. Riedel, *Solid State Ionics*, 2012, **225**, 527-531.
12. L. David, R. Bhandavat, U. Barrera and G. Singh, *Nat Commun*, 2016, **7**.
13. P. Colombo, G. Mera, R. Riedel and G. D. Soraru, *J. Am. Ceram. Soc.*, 2010, **93**, 1805-1837.
14. G. M. Renlund, S. Prochazka and R. H. Doremus, *J. Mater. Res.*, 1991, **6**, 2716-2722.
15. H. Zhang and C. G. Pantano, *J. Am. Ceram. Soc.*, 1990, **73**, 958-963.
16. G. M. Renlund, S. Prochazka and R. H. Doremus, *J. Mater. Res.*, 1991, **6**, 2723-2734.
17. G. D. Soraru, G. D'Andrea, R. Campostrini, F. Babonneau and G. Mariotto, *J. Am. Ceram. Soc.*, 1995, **78**, 379-387.
18. M. Wilamowska, V. S. Pradeep, M. Graczyk-Zajac, R. Riedel and G. D. Soraru, *Solid State Ionics*, 2014, **260**, 94-100.
19. L. David, K. M. Shareef, M. A. Abass and G. Singh, *RSC Advances*, 2016, **6**, 53894-53902.
20. H. Konno, T. Morishita, S. Sato, H. Habazaki and M. Inagaki, *Carbon*, 2005, **43**, 1111-1114.
21. H. Fukui, H. Ohsuka, T. Hino and K. Kanamura, *Chem. Lett.*, 2009, **38**, 86-87.
22. D. Ahn and R. Raj, *J. Power Sources*, 2010, **195**, 3900-3906.
23. H. Fukui, O. Hisashi, T. Hino and K. Kanamura, *ACS Appl. Mater. Interfaces*, 2010, **4**, 998-1008.
24. V. S. Pradeep, M. Graczyk-Zajac, R. Riedel and G. D. Soraru, *Electrochim. Acta*, 2014, **119**, 78-85.
25. H. Fukui, Y. Harimoto, M. Akasaka and K. Eguchi, *ACS Appl. Mater. Interfaces*, 2014, **6**, 12827-12836.
26. H. Fukui, H. Ohsuka, T. Hino and K. Kanamura, *J. Electrochem. Soc.*, 2013, **160**, A1276-A1281.
27. P. E. Sanchez-Jimenez and R. Raj, *J. Am. Ceram. Soc.*, 2010, **93**, 1127-1135.
28. P. Kroll, *MRS Online Proc. Libr.*, 2011, **1313**, 1-6.
29. N. Liao, B. Zheng, M. Zhang and W. Xue, *J. Mater. Chem. A*, 2016, **4**, 12328-12333.
30. H. Sun and K. Zhao, *ACS Appl. Mater. Interfaces*, 2017, **9**, 35001-35009.
31. M. Narisawa, F. Funabiki, A. Iwase, F. Wakai and H. Hosono, *J. Am. Ceram. Soc.*, 2015, **98**, 3373-3380.
32. M. Narisawa, A. Iwase, S. Watase, K. Matsukawa and T. Kawai, in *Innovative Processing and Manufacturing of Advanced Ceramics and Composites II*, John Wiley & Sons, Inc., 2014, DOI: 10.1002/9781118771464.ch7, pp. 79-84.
33. P. S. Waleska and C. Hess, *J. Phys. Chem. C*, 2016, **120**, 18510-18519.

34. A. Sadezky, H. Muckenhuber, H. Grothe, R. Niessner and U. Poeschl, *Carbon*, 2005, **43**, 1731-1742.
35. A. C. Ferrari and J. Robertson, *Phys. Rev. B*, 2001, **64**, 075414-075414.
36. C. Castiglioni, M. Tommasini and G. Zerbi, *Philos. Trans. R. Soc., A*, 2004, **362**, 2425-2459.
37. J. Kaspar, M. Graczyk-Zajac and R. Riedel, *J. Power Sources*, 2013, **244**, 450-455.
38. S. J. Widgeon, S. Sen, G. Mera, E. Ionescu, R. Riedel and A. Navrotsky, *Chem. Mater.*, 2010, **22**, 6221-6228.
39. A. Grill and D. A. Neumayer, *J. Appl. Phys.*, 2003, **94**, 6697-6707.
40. M. Narisawa, K. Terauds, R. Raj, Y. Kawamoto, T. Matsui and A. Iwase, *Scripta Mater.*, 2013, **69**, 602-605.
41. G. Socrates, *Infrared and Raman Characteristic Group Frequencies: Tables and Charts*, Wiley, 2004.
42. E. Zera, W. Nickel, S. Kaskel and G. D. Soraru, *J. Eur. Ceram. Soc.*, 2016, **36**, 423-428.
43. H. Bréquel, J. Parmentier, S. Walter, R. Badheka, G. Trimmel, S. Masse, J. Latournerie, P. Dempsey, C. Turquat, A. Desmartin-Chomel, L. Le Neindre-Prum, U. A. Jayasooriya, D. Hourlier, H. J. Kleebe, G. D. Sorarù, S. Enzo and F. Babonneau, *Chem. Mater.*, 2004, **16**, 2585-2598.
44. C. Castiglioni and M. Tommasini, *Opt. Pura Apl.*, 2007, **40**, 169-174.
45. A. C. Ferrari and J. Robertson, *Mater. Res. Soc. Symp. Proc.*, 2000, **593**, 299-304.
46. A. C. Ferrari and J. Robertson, *Phys. Rev. B*, 2000, **61**, 14095-14107.
47. C. Tyborski, F. Herziger, R. Gillen and J. Maultzsch, *Phys. Rev. B*, 2015, **92**.
48. F. Roth, P. Waleska, C. Hess, E. Ionescu and N. Nicoloso, *J Ceram Soc Jpn*, 2016, **124**, 1042-1045.
49. H.-J. Kleebe, C. Turquat and G. D. Soraru, *J. Am. Ceram. Soc.*, 2001, **84**, 1073-1080.
50. G. Gregori, C. Turquat, H.-J. Kleebe and G. D. Soraru, *Key Eng Mat*, 2002, **206**, 2061-2064.
51. H. Fukui, H. Ohsuka, T. Hino and K. Kanamura, *J. Power Sources*, 2011, **196**, 371-378.
52. H. Fukui, K. Eguchi, H. Ohsuka, T. Hino and K. Kanamura, *J. Power Sources*, 2013, **243**, 152-158.
53. M. Haaks, J. Kaspar, A. Franz, M. Graczyk-Zajac, R. Riedel and M. Vogel, *Solid State Ionics*, 2016, **287**, 28-35.
54. L. M. Reinold, Y. Yamada, M. Graczyk-Zajac, H. Munakata, K. Kanamura and R. Riedel, *J. Power Sources*, 2015, **282**, 409-415.